Motion Characteristics of a Modularised Floating Solar Farm in Waves

Yujia Wei[a], Detai Zou[a, b], Deqing Zhang[c], Chao Zhang[b], Binjian Ou[a], Soegeng Riyadi[d], I.K.A.P. Utama[e], Wolter Hetharia[f], Tim Wood[g], Luofeng Huang[a, *]

[a]School of Water, Energy and Environment, Cranfield University, Cranfield MK43 0AL, UK

[b]Department of Mechanical Engineering, Jiangsu University, Zhenjiang 212013, China

[c]College of Engineering, Ocean University of China, Qingdao 266100, China

[d]PT Orela Shipyard, Jl Raya Ngemboh RT2RW1, Kab.Gresik 61154, Indonesia

[e]Department of Naval Architecture, Institut Teknologi Sepuluh Nopember, Surabaya 60111, Indonesia

[f]Department of Naval Architecture, University of Pattimura, Ambon 97223, Indonesia

[g]Achelous Energy Limited, Unit 2 Black Robins Farm, Edenbridge TN8 6QP, UK

*Corresponding author: luofeng.huang@cranfield.ac.uk (L. Huang)

Abstract

Modularised floating solar farm exhibits the potential to replace conventional steel-frame ones, effectively remedying hydroelastic issues of a very large floating structure through discrete modules with mechanical connections. However, the response of the discrete modules under cyclic loading has not been fully understood. This paper assesses the motion characteristics and expansibility of modularised floaters in waves, based on computational results from fluid-structural interaction simulations. A crucial factor, denoted as the ratio of frame length to wavelength $R = L_s/\lambda$, is determined to predict the motions of a large floating solar system in head waves. Results indicate a significant impact on vertical motions, which is predictable based on the R value. The empirical relationship between the R value and the motion of every unit in an array is ascertained. In particular, the results calculated from using the multiple-rigid-bodies method are also compared with those from using the single-large-hydroelastic-body method, and it was found that these two results are similar when R > 1. This similarity allows for predicting the multi-hinged bodies' behaviour in waves through a simplified hydroelastic approach. The reported insights are useful for the design and optimisation of modularised solar farms, and can help address cyclic load and motion concerns for long-term durability.

Keywords: Floating solar; modularised floating structures; fluid-structure interactions; motion; vibration; multibody dynamics.

1. Introduction

Floating Photovoltaic (FPV) systems have gained prominence as efficient and sustainable renewable energy sources, offering advantages like minimal land use, higher power generation efficiency, and environmental preservation (Kjeldstad et al., 2021) (Kjeldstad et al., 2022). Recent review papers have reported floating solar as a fast-progressing research direction and identified a range of practical challenges and future directions (Cazzaniga & Rosa-Clot, 2021) (Claus & López, 2022) (Shi et al., 2023). While traditional solar farms are often deployed on calm water bodies, the growing demand for FPV systems in nearshore or deep sea areas introduces complexities, including the impact of wind and waves on structural stability (Sahu et al., 2016) (Dai et al., 2020; Essak & Ghosh, 2022) (Jiang et al., 2023) (Bi & Law, 2023) (Esparza et al., 2024).

Recent years have seen a transition from integrated FPV structures (Cazzaniga & Rosa-Clot, 2021) to modular designs that consist of numerous floating units connected through joints. The modularised systems offer advantages such as scalability, straightforward assembly, and easy maintenance for localised items (Essak & Ghosh, 2022) (Wang & Lund, 2022). They also help minimize hydroelastic structural issues compared to integrated single structures (Cazzaniga et al., 2018). These advancements support the planning and deployment of FPV in wave environments, e.g. coastal and offshore regions (Sree et al., 2022) (Shi et al., 2023). Ensuring the

safety and long-term reliability of components in large-volume floating solar farms is critical (Choi & Lee, 2015). The interaction between ocean waves and modular solar systems introduces nonlinearities due to the dynamics of multiple bodies and their internal interactions (Cao et al., 2021) (Li et al., 2023). Understanding and predicting such systems during the design stage becomes challenging, particularly when considering various excitation sources and mooring systems.

Previous hydrodynamic interaction research has relied on potential flow theory, with studies dating back to the 1970s. Ohkusu (1976) developed an approach to predict the wave forces and moments on multi-row floating bodies, based on 2D potential flow theory. Since then, a similar approach has been adopted by a great deal of research which focused on the hydrodynamic interaction of multiple floating bodies using either 2D (Fang & Kim, 1986) or 3D potential methods (Hong et al., 2005) (Zhu et al., 2008) (Ikhennicheu et al., 2022) (Wang et al., 2022) (Li & Liu, 2022). The good agreement between their results and model tests illustrated that potential flow theory is a simple and effective method for predicting the hydrodynamic interaction of multiple structures.

Although high-fidelity methods, i.e., Finite Volume methods (FVM), are widely used in wave structure interaction problems, they are often limited in scale. These methods provide accurate evaluations of the flow field by considering fluid viscosity, making them suitable for gap resonance problems involving multiple bodies (Feng et al., 2017) (Dafnakis et al., 2020). However, their applications become challenging and impractical for floaters with hundreds or thousands of connections, given their high computational costs and numerical difficulties. Several research papers have explored simulating the hydrodynamics of multi-floating structures using Computational Fluid Dynamics (CFD) methods, focusing on applications like array-breakwater (Wang et al., 2023), and deformable Very Large Floating Structures (VLFSs) (Wei et al., 2024a). However, these simulations reveal limitations in accurately representing large arrays. As solar farm scales increase, the feasibility of accounting for viscous flow diminishes due to the computational demands associated with mesh-type modelling.

A review of existing research on the motion characteristics of Modularised Floating Solar (MFS) reveals a predominant limitation in terms of array length or floater numbers, resulting in a case-by-case analysis. Notably, studies often focus on single arrays, examining free floats (Zhang et al., 2022) or hinged configurations (Zhang et al., 2023). While these investigations yield valuable insights, such as the determination of radiational radius factors and motion behaviours, their extension to large arrays raises questions. Wave diffraction tends to be exaggerated for single arrays compared to multi-arrays, and the wave transmission shapes differ significantly due to blocking and trapping effects among parallel modules. Additionally, optimization procedures for MFS configurations have been explored (Michailides et al., 2013), taking into account various module layouts (grid type) and mechanical properties based on performance criteria. These findings hold potential value for designing floater deployment connection methods under diverse environmental conditions. However, the need for comprehensive studies encompassing larger arrays and considering the intricate dynamics of modularised solar farms remains evident, urging further exploration in this direction.

The challenge of understanding the motion characteristics of a solar farm primarily stems from the intricacies of multibody dynamics, even when excluding water effects. From a structural vibration perspective, such a system, under a single excitation, exhibits varied responses due to the multiple constraints, resembling the behaviour of a continuum structure. In elastic bodies, different eigenvalues and modes emerge at various excitation frequencies. To address this complexity, this study proposes a bold hypothesis, treating a multi-body articulated system akin to an elastic body system. This approach draws inspiration from the work of (Newman, 1997; Newman, 1994) (Newman, 2005), specifically focusing on the hydroelastic response of hinged and deformable bodies. By considering the continuous discretized form of hinged bodies, this hypothesis anticipates similar physical trends in the multi-body motion of solar farms in waves, aligning with hydroelasticity principles.

Limited recent research in MFS industries, exemplified by (Delacroix et al., 2023) has delved into the exploration of multibody articulated systems. Delacroix et al. identified a first-order pitch resonant mode excitation in such systems when wavelengths are approximately twice the floater's length, providing valuable insights for the initial design of floating solar farms. However, the explanations for the observed phenomena remain lacking. Additionally, Ren et al. (2019) highlighted the sensitivity of MFS hydrodynamic responses to connector types, wave phase, and wavelength.

This study fills the research gap concerning the limitations of multibody dynamics principles in representing complex interactions between discrete floating bodies. The work proposes an innovative parameterisation that considers the relationship between the ratio of structure length to wavelength and the floating-body motions. This approach offers potential generalisation for predicting and understanding the motion characteristics of solar farms in wave conditions. The results can be particularly useful to facilitate the initial design stage of floating solar farms. The paper also compares an array of structures' motion as the superposition of inherent vibration modes and has found similarities with existing hydroelastic theories, which have not been discussed in existing literature.

The structure of this paper is organised as follows: Section 2 outlines the modularised solar farm concept. Section 3 introduces the simulation model and its governing equations. Section 4 presents verification of the established model. In Section 5, we delve into the floating solar array's motion characteristics in waves through various parametric studies, considering wave conditions and array arrangement. Also, a vibration analysis is conducted to enhance structural understanding. The paper is summarised in Section 6 with its conclusions, limitations and recommendations for future work.

2. Modularised solar farm

The hydrodynamic analysis is conducted on a modularised floating solar farm, with the representative model consisting of $M \times N$ floaters (13×7), as shown in Figure 1. The chosen maximum array size of 13×7 was selected based on preliminary simulations showing that this array size is sufficiently large that further increasing the size of the array would give similar conclusions. The whole framework extends along the $x - y$ plane within a range of $-11.0\ m < x_s < 11.0\ m$ and $-4.185\ m < y_s < 4.185\ m$. Each individual floater has a length L_i of 1.6 m and a width D_i of 1.1 m. The draft T_i is fixed at 0.1, determined by the weight of each floater. A Cartesian coordinate system ($O - XYZ$) is used, where $Z = 0$ indicates the undisturbed free surface. Inside of coordinate, X sets positive toward the 'wave facing' of the array, Y is positive toward the port side, and Z is positive upwards. The incident wave direction β is assumed as the angle between the wave propagation direction and the positive X-axis, with $\beta = 0°$ corresponding to the head wave.

Simple transverse hinge joints are placed longitudinally between every two floaters of the array at the calm waterline, with a distance of $(L_i + \frac{d}{2}) \times$ m, where d is the gap between floaters and m ranges from 1 to $M - 1$. The hinges only allow pitch rotational motions R_{yy} between the connected two floaters, and the axes of the hinged joints are parallel to Y-axis. In the OY direction, rod elements are implemented to connect floaters in the normal direction with distances $(D_i + \frac{d}{2}) \times n$, where n ranges from 1 to $N - 1$. The rod connection is achieved by using a combination of fender and linear cable elements to prevent the local contact and locking effect. The geometric characteristics of these mechanical connections are assumed dimensionless without consideration of added weight.

The inclusion of hinge and rod connections in the MFS system improves flexibility and reduces the local bending moments caused by wave loads. The physical parameters, such as the stiffness of the hinge and rod, are summarised in Table 1. These stiffness values are chosen to allow flexibility in relative motions between floaters, while avoiding excessively low values that could result in the floaters reacting as an integrated structure. Although the current stiffness values aim to prevent significant resonance issues, further optimisation could be achieved through fine tuning this parameter. It is worth noting that the stiffness could be automatically adjusted in real-time according to the motion amplitudes (Anderlini et al., 2020), which could be potentially applied to FPV.

In this study, the selection of the gap d between adjacent floaters take into account floater size, relative motions, and potential resonance effects of narrow gap, as discussed by (Liu et al., 2022). The preliminary design selects the d as a constant value of 0.1 m. The mooring system, represented by a linear spring model, is equipped as shown in the figure. At each end side, two symmetric mooring lines at an angle of 60° are connected the central and rear floater to vertical piles ($z = -5\ m$). Mooring anchor points are located on these piles. Pretensions are applied to the mooring lines based on the relation between distance and stiffness.
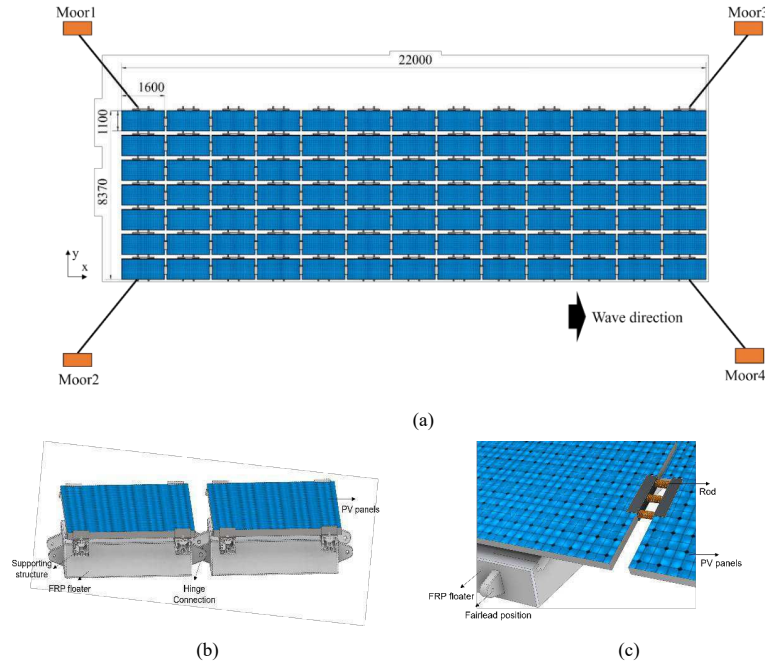
(a)

(b)

(c)

Figure 1: Sketch of modularised floating solar farm with hinge connections, (a) Framework, (b) Rod connections, (c) Hinge connections.

Table 1: Physical properties of the selected floater and mechanical connections.

Floater	Unit	Value	Mechanical connections	Unit	Value
Length L	(m)	1.8	Hinge stiffness	(N/m)	-
Width D	(m)	1.1	Rod stiffness	(N/m)	$1e^6$
Draft T	(m)	0.2	Mooring stiffness	(N/m)	$1e^8$

3. Governing equations

3.1 Fluid solution

Assuming the surrounding fluid is ideal, the velocity potential that satisfies the Laplace equation in the whole fluid is introduced. With floating bodies in the wave field, the propagation of the incident waves will be affected, the isolated space dependent potential term $\varphi(\vec{X})$ may be separated into contributions from the incident wave potential ϕ_I, the diffracted wave potential ϕ_D and the radiation wave potential ϕ_R. The pressure distribution (p) on the wet surface can be obtained by the linearized Bernoulli equation:

$$p = -\rho g z - \rho\left(\frac{\partial \phi_I}{\partial t} + \frac{\partial \phi_D}{\partial t} + \frac{\partial \phi_R}{\partial t}\right) \tag{1}$$

Inside the equations, the linearized incident wave velocity potential φ_I is described as

$$\varphi_I = -\frac{ig\eta_0}{\omega_0}\frac{coshk(z+d)}{coshkd}e^{i[k(xcos\beta+ysin\beta)]} \tag{2}$$

where ρ is the fluid density, d refers to the water depth, β is the angle of wave heading, and k is the wave number.

The radiation potential can be solved by Green's function method and the radiation force can be expressed as (Cummins, 1962)

$$F_{k,R}(t) = -\int_s \rho \frac{\phi_R(t)}{\partial t} n_k ds = -\sum_{j-1}^{6N}[m_{kj}\ddot{\xi}_j(t) - \int_{-\infty}^{t}\dot{\xi}(t)K_{kj}(t-\tau)dr] \quad (3)$$

where $\ddot{\xi}_j$ indicates the acceleration, n_k is the external normal vector of a point on the module surface, N is the number of modules, k and j at subscript represents the k-th module in the j-th DOF(Degree of freedom), m_{kj} and $K_{kj}(t)$ are the additional coefficient and delay function coefficient, respectively.

$$K_{kj}(t) = \frac{2}{\pi}\int_0^\infty B_{kj}(\omega)\cos(\omega t)\,d\omega \quad (4)$$

where $B_{kj}(\omega)$ is the radiation damping derived through frequency domain analysis. From the pressure distribution, the various fluid forces may be calculated by integrating the pressure over the wetted surface of the body. The hydrostatic restoring force $F_{k,HS}$ can be expressed as:

$$F_{k,HS} = -C_{kj}\xi_j(t) \quad (5)$$

where C_{kj} is the hydrostatic force coefficient.

3.2 Structural solution

The motion prediction of a multi-connected system, as shown in Figure 2, can be calculated with the consideration of the connection system (i.e., line $F_{k,line}$ and fender $F_{k,fender}$) and mooring system ($F_{k,moor}$) as shown in the following time-domain mode:

$$\sum_{j=1}^{6N} M_{kj}\ddot{\xi}_j(t) = F_{k,wave}(t) + F_{k,line}(t) + F_{k,moor}(t) + F_{k,fender}(t) \quad (6)$$

For the hinge constraint bodies, the boundary condition is given for while only one rotational freedom exists and there is no relative translational motion at the articulated joint between the linked structures. in this case, hinge is applied in the x-direction, Denoting $\vec{X}_{gk}, \vec{X}_{gk1}$ as the locations of the centre of gravity of the k-th and $(k+1)$-th structures respectively using the following generalized form:

$$\begin{bmatrix} E^T & E^T R_k \\ 0 & G^T \end{bmatrix} U_k - \begin{bmatrix} E^T & E^T R_{k1} \\ 0 & G^T \end{bmatrix} U_{k1} = 0 \quad (7)$$

Where Euler rotational matrix E, R_k and R_{k1}, hinge matrix G are expressed as

$$E = \begin{bmatrix} e_{11} & e_{12} & e_{13} \\ e_{12} & e_{22} & e_{23} \\ e_{13} & e_{32} & e_{33} \end{bmatrix}, R_k = \begin{bmatrix} 0 & z_k & -y_k \\ -z_k & 0 & x_k \\ y_k & -x_k & 0 \end{bmatrix}, R_{k1} = \begin{bmatrix} 0 & z_{k1} & -y_{k1} \\ -z_{k1} & 0 & x_{k1} \\ y_{k1} & -x_{k1} & 0 \end{bmatrix}, G = \begin{bmatrix} e_{11} & 0 & e_{13} \\ e_{12} & 0 & e_{23} \\ e_{13} & 0 & e_{33} \end{bmatrix} \quad (8)$$
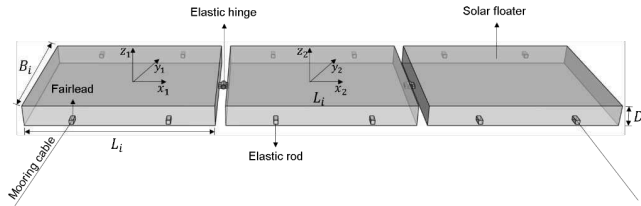
$$U_k = (\vec{u}_k, \vec{\theta}_k), U_{k1} = (\vec{u}_{k1}, \vec{\theta}_{k1}) \quad (9)$$

where u and θ are the translation and rotational displacements, the vectors between the joint point are written as

$$\vec{r}_k = \vec{X}_p - \vec{X}_{gk} = (x_k, y_k, z_k) \quad (10)$$

$$\vec{r}_{k1} = \vec{X}_p - \vec{X}_{gk1} = (x_{k1}, y_{k1}, z_{k1}) \quad (11)$$

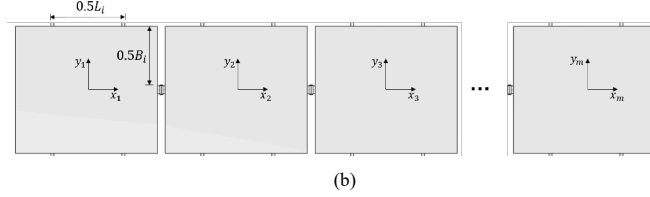where $\vec{X}_p$ is the connection point in the global axis.

(a)

Figure 2: The sketch of multi-hinged structure, (a) Front view, (b) Plan view.

- Line and fender elements

The linear elastic rod is defined by the combination of line and fender system, which provides axial stress and stiffness from stretch and compression. The line $F_{k,line}$ and fender forces $F_{k,fender}$ can be calculated as:

$$F_{k,line} = \begin{cases} K_l(L_l - L_{l0}) \; if \; L_l > L_{l0} \\ 0 \qquad\qquad if \; L_l \leq L_{l0} \end{cases} \tag{12}$$

$$F_{k,fender} = \begin{cases} K_f(L_{f0} - L_f) \; if \; L_f > L_{f0} \\ 0 \qquad\qquad if \; L_f \leq L_{f0} \end{cases} \tag{13}$$

where, K_l and K_f are the stiffness of the line and fender, respectively; L_l and L_{l0} denote the instantaneous and unstretched length of the linear cable, similarly L_f and L_{f0} represents the length of fender element.

- Mooring system

The tension type of mooring system is modelled using a linear elastic cable, which the mooring force $F_{k,moor}$ is calculated based on the stiffness, initial unstarched length, and two attachment points of the mooring line, which can be calculated as:

$$F_{k,moor} = \begin{cases} K_m(L_m - L_{m0}) \; if \; L_m > L_{m0} \\ 0 \qquad\qquad if \; L_m \leq L_{m0} \end{cases} \tag{14}$$

where the stretched length of mooring line can be calculated based on the relative distance between the anchor and fairlead points $L_m = [\vec{X}_1(t) - \vec{X}_2(t)]$.

To solve the motion equation (Eq. 6), it is necessary to obtain the wave excitation force matrix, hydrostatic force matrix, additional mass matrix and radiation damping matrix. These matrices can be obtained through frequency domain analysis using (AQWA Line). Then, simulate using AQWA Naut (regular wave) with the Newmark-Beta numerical method.

One challenge in solving the hydrodynamic interaction problem in potential flow theory is the occurrence of fluid resonance phenomenon in the gap between adjacent bodies. This phenomenon is caused by the absence of viscous flow effects. To mitigate unrealistic shocking wave phenomena in the analysis, a lid-type free-surface boundary is required. This boundary helps dampen the free-surface nonlinearity between adjacent structures. This condition is expressed as:

$$\frac{\omega^2}{g}(a^2 f_1 - 1)\phi - 2i\frac{\omega^2}{g}af_1\phi + \frac{\partial\phi}{\partial z} = 0 \; where \; z = 0 \tag{15}$$

$$f_1 = \begin{cases} sin^2\left(\frac{\pi}{2}\frac{\omega}{\omega_0}\right) where \; \omega < \omega_0 \\ \left(\frac{\omega}{\omega_0}\right)^2 \qquad where \; \omega \geq \omega_0 \end{cases} \tag{16}$$

$$\omega = \sqrt{\frac{g}{\frac{d*L}{h-d}+d}} \tag{17}$$

$$\omega_0 = max\left\{0.1, \sqrt{\frac{\pi g}{d}}\right\} \tag{18}$$

where ω is the pumping mode frequency, d represents gap width, L is the floating body length, d denotes water depth, and ω_0 is the critical frequency occurs at $\sqrt{\frac{g}{d}}$, a is the damping factor, f_1 is a function that relates to the gap width.

4. Verification

Verification of the hydrodynamic performance of multiple unconnected floaters is conducted to ensure accurate modelling of the selected computational solver on the dynamic structural motions in the wave-structure problems. The potential flow model is established in Ansys AQWA and detailed configuration remains consistent with literature from (Chen et al., 2021; Chen et al., 2023). The model consists of several identical rectangular floaters as shown in Figure 3, with parameters summarised in Table 2. The floaters are symmetric along both x and y axes, and incident head waves are considered. The centre of gravity of the single floater is located at its geometric centre and the mass is assumed to be uniformly distributed. The water depth is 50 m. Given that the head sea ($\beta = 0°$) is the main wave condition considered, the three modes of motion including surge, heave, and pitch under various heading wave frequencies are the main focus of this study.
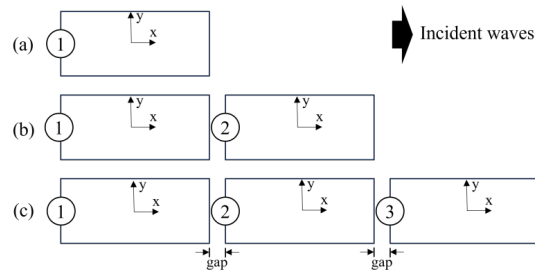

Figure 3: Plan view of three configurations (a) 1 module, (b) 2 modules, (c) 3 modules.

Table 2. Geometrical parameters of a single floater

Module characteristics	Unit	Value
Length	m	100
Breadth	m	50
Depth	m	5
Centre of gravity above base, KG	m	2.5
Draught	m	2
Moment of inertia, I_{xx}	m^4	14.5
Moment of inertia, I_{yy}	m^4	28.9
Moment of inertia, I_{zz}	m^4	32.3

In Figure 4, the Response Amplitude Operators (RAOs) of each windward module of the three models (a, b, c) is compared to the literature (Chen et al., 2021). To highlight the hydrodynamic interactions between multiple bodies, the response amplitudes of different numbers of floaters are plotted in the figure using various lines and symbols. Among them, the pitch response curves appear largely influenced by the increase of module number, the peak magnitudes reduce from one to three in the range of 0.5– 1 rad/s. The displacement results are somewhat different. Strong nonlinearity induced by the fluid-structure interaction can be observed in short waves $f = $ 1.5– 2 rad/s, leading to higher computational deviation. The good agreement between their results and model

tests illustrated that potential flow theory is a simple and effective method for predicting the hydrodynamic interaction of multiple structures in waves. However, due to the inviscid flow assumption, special care should be taken with the added damping factor to avoid overestimating the interaction effect in certain frequency ranges. The mean deviation between the response amplitude from the present model and the literature is calculated in Table 3. As expected, the numerical error induced by pitch motions is generally higher than that induced by displacement motions. This is because the rotational motion is affected by changes in the wet surface area, which may not be effectively calculated based on the Green function method.

(a)

(b)

(c)
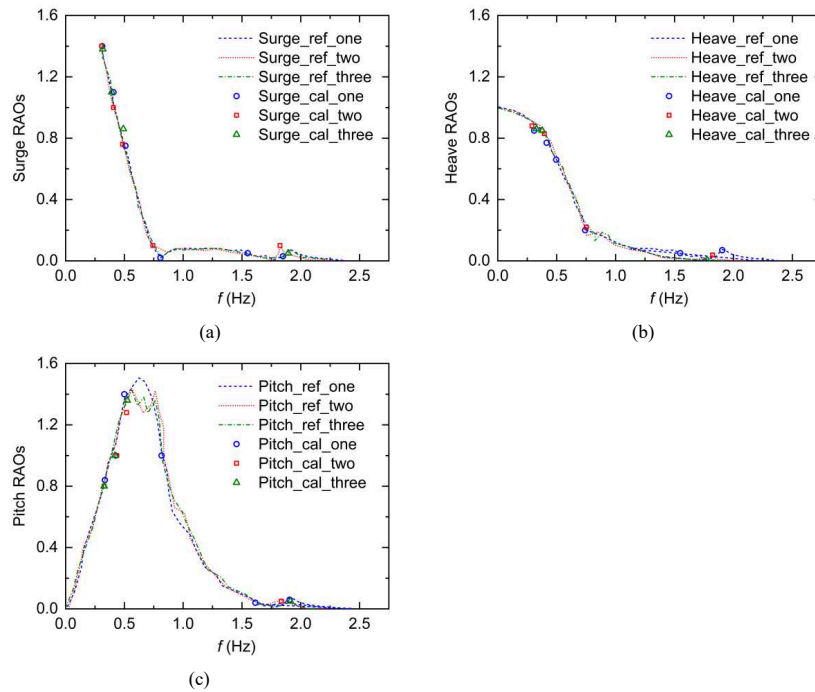
Figure 4: RAOs of the multi-floaters under various wave conditions. (a) Surge, (b) Heave, (c) Pitch

Table 3. Uncertainty evaluations on structural motions.

Uncertainty level	One	Two	Three
Mean surge RAOs	4.6%	3.7%	2.9%
Mean heave RAOs	1.4%	5.2%	6.74%
Mean pitch RAOs	9.5%	9.5%	14.4%

5. Results and Discussion

5.1 Vertical motion evaluation in arrays

In this section, the previous numerical model is further expanded to include the hydrodynamic analysis of 7×7 arrays of floaters under various heading wave conditions (T=1.45 s-2.06 s). The detailed joint connections and mooring system are similar to those attached in Section 2 previously. Since the focus of this research is on

hydrodynamic motions, the number of motion degrees of freedom (DoFs) for each body can be reduced to only consider surge, heave, and pitch. All these computational results have been non-dimensionalised and are independent of specific scales or units and facilitate the application of the findings to different scales or sizes in real-world scenarios.

As the evidence in Section 4.2 indicates, when the number of discrete objects is large and the link structure is relatively flexible, multi-connected systems can result in motion characteristics similar to those of a continuum. Therefore, in Figure 5, the plane contour illustrates the non-dimensional heave results of the array with six wave frequencies. The RAO values are calculated based on the time-average vertical motion of floaters in each row (x) and column (y) over 30 seconds, and then dividedby the incident wave amplitude. Ratio of Structure (ROS) represents the ratio between an individual floater length to wavelength. It is seen that the heave motion of the system exhibits a single harmonic with a magnitude close to 1. This behavior is similar to that of a rigid body when L_s is much smaller than λ. In contrast, short waves have a large impact on the wave-wards region of the array and decrease as they propagate, representing energy loss due to blocking, shielding and gap effects. This phenomenon is depicted in Figure 5(a-d), where significant motion (shown in red) is detected in the front arrays, leaving blank regions (shown in purple) towards the end arrays. Another finding is found in the columns associated with mooring attachment (C1 and C7), where relatively larger vertical motions are observed compared to the internal regions. However, this phenomenon may be altered with different mooring configurations.
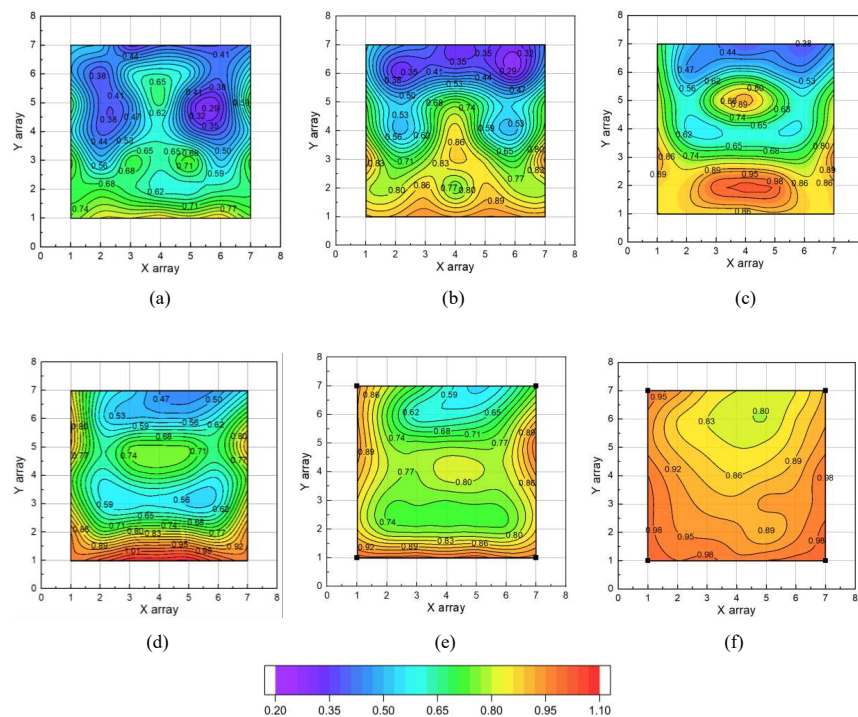

Figure 5: Heave RAOs distribution within the array 7×7 under various wave conditions (a) T=1.533s, ROS=0.3, (b) T=1.68s, ROS=0.25, (c) T=1.878s, ROS=0.2, (d) T=2s, ROS=0.15, (e) T=2.67s, ROS=0.1, (f) T=3.98s, ROS=0.05.

In the early stages of MFS system design, it is reasonable to evaluate its motion characteristics based on regular wave theory, before considering the geographical and operating conditions of the deployment sea area. This can be done by superimposing the heave RAOs with a series of wave frequencies and calculating their mean value

(Figure 6a) to illustrate a relatively generalized heave field (Fig. 6b). By employing this approach, the heave distribution of the array can be determined independently of specific wave conditions, which is particularly advantageous when a predefined wave spectrum has not yet been identified.

The figures first reveal that severe vertical motion is primarily experienced by wave-facing arrays, irrespective of specific wave conditions, aligning with previous findings. This observation emphasizes the possibility of implementing protective measures, such as the installation of a breakwater, to mitigate direct contact between water and solar panels, thereby addressing the challenges posed by significant motions in these specific arrays.

Furthermore, the array demonstrates symmetric structural behaviour along its middle column (Column 4). This symmetry is evident in the corresponding pattern of the structure on both sides, where the numerical error of structural imbalance resulting from wave diffraction is minimal. Figure 6(b) specifically highlights the occurrence of peak heave motion at the centre of the array. This phenomenon may be attributed to wave-structure resonance within the array. However, it is important to note that the current array, consisting of only seven floaters in a row or column, may not sufficiently represent the overall characteristics for larger volume scenarios. Therefore, the expandability of the array is further explored in the subsequent section.
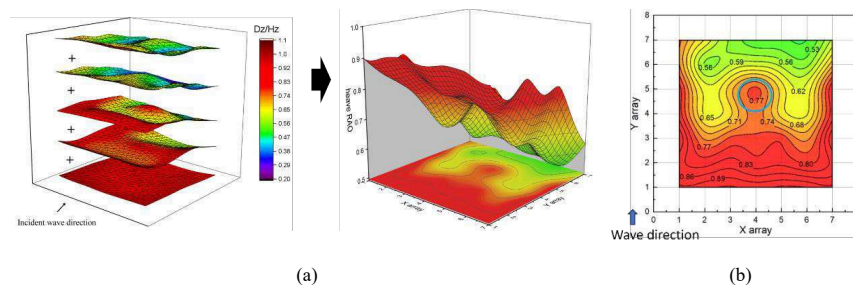

| (a) | (b) |

Figure 6: Heave RAOs distribution of the array 7×7, (a) superposition of results from multiple wave conditions, (b) 2D plane view.

5.2 Vibration analysis on heave motions

The volume of MFS is influenced by the installed capacity. In practical deployments, the number of solar panels can reach several thousand, causing the longitudinal dimension to significantly extend over the water's free surface in a geometric manner. To investigate the scalability of the MFS, the number of floaters considered for the cases increases from 7 to 13 in the wave propagation direction, while keeping the number of floaters at 7 in the normal wave direction.

The ultimate frame in longitudinal with 13 floaters has been found to effectively dissipate waves as they reach the end of the array, with no noticeable disturbance from the wave to the end structures. This is mainly due to the current model settings, where wave energy is mostly absorbed through diffraction, allowing only a relatively small wave amplitude to be transmitted to the ends. However, this phenomenon depends on several factors, including the selected wave height, floater draft, and arrangement properties. By altering these key factors, the wave transmission performance in relation to structural geometry may change accordingly.

The time-averaged heave RAOs are calculated for each deployment based on five different wave frequencies ($f = 0.48, 0.53, 0.59, 0.65, 0.714$ Hz), as shown in the contour plots in Figure 7. It can be observed that as the number of floaters increases, the overall motion characteristics of the system tend to become similar to each other (Figure 7(c, d)). The motion in the longitudinal direction exhibits a gradient reduction, with the highest motion occurring mostly at the wave-facing region and gradually decreasing towards the end columns. However, noticeable multiundulating shapes are observed internally within the array, indicating the emergence of nonlinearity resulting from the complex structural interactions within the multi-body system.
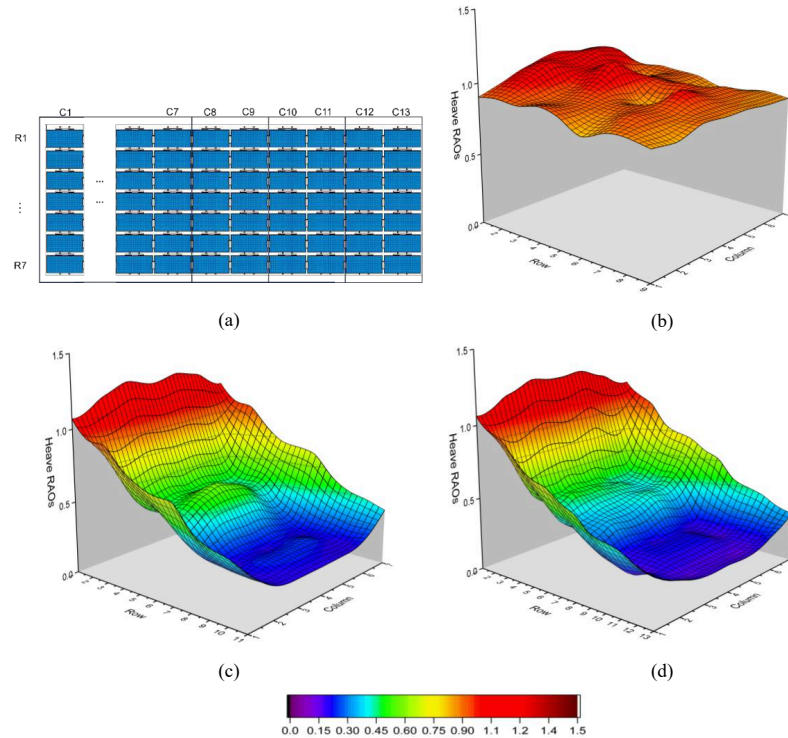
Figure 7: Heave RAOs analsysis on the longitudinal expandability of hinged-arrays, (a) Model description, (b) Results of a 9×7 Array, (c) Results of a 11×7 array, (d) Results of a 13×7 array.

Analysing vibration behaviours is crucial for understanding a multi-hinged system with single harmonic excitation. Such multi-body systems introduce high complexity due to added mechanical connections, resulting in a diverse range of frequencies. This poses a challenge in accurately predicting motion, even when the external excitation is uniform. The eigenmodes of the system are often associated with the inherent vibration eigenshapes and are affected by resonances from the interconnected bodies.

Figure 8 first assesses the motion shapes of a frame column (C1) within the cases of four expand abilities (M=7-13) on the shortest heading wave ($f = 0.714$Hz), and real-time heave data are extracted with four even time frames in a wave cycle ($0.25T$, $0.5T$, $0.75T$, T). When the length of an array increases, it is observed that the motion patterns resemble wave shapes, with distinct peak and trough values that align with wave characteristics. This motion can be visualized as a flexible map moving along with free surface waves. The distances between peak-to-peak of the array are highlighted in the figure, which directly corresponds to the incident wavelength, regardless of the expandability of the array.

It is important to note that these phenomena are only evident when the length of the array is significantly larger than the wavelength (i.e., $\frac{L_S}{\lambda} > 2$). In shorter waves, wave interference may diminish the visibility of these phenomena. Over time, a phase lag ($1/4T$) is observed, aligning with the waves in each time slot. However, the motion magnitudes of the longitudinal array generally occur as it sweeps or vibrates through $z = 0$, where it crosses 0 between positive and negative values and eventually reaches a constant value. This value exhibits a decreasing trend as it propagates in the direction of the waves, which can be attributed to blocking effects.
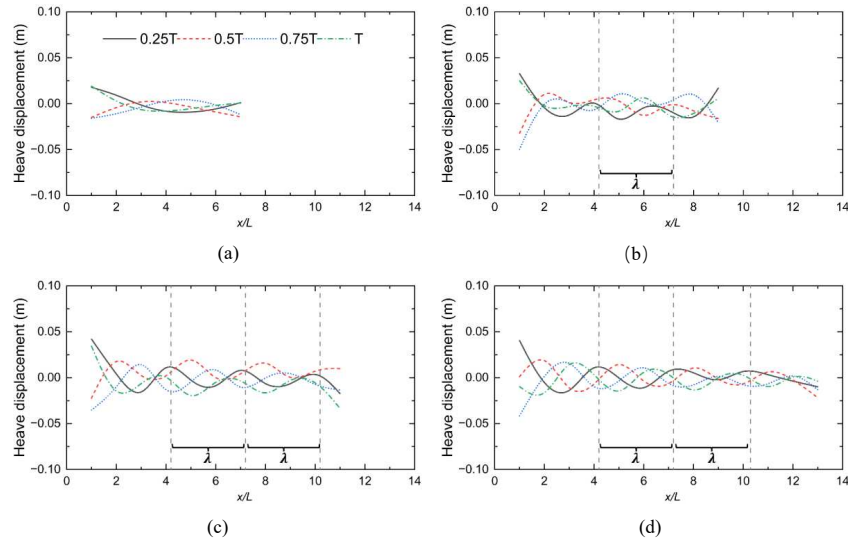
Figure 8: Heave trajectory in longitudinal with four time frames at wave period $T = 1.45$s, (a) Results of a 7×7 array, (b) Results of a 9×7 array, (c) Results of a 11×7 array, (d) Results of a 13×7 array.

Figure 9 evaluates the vibration behaviours on the frame column (C1) of the longest array (13×7) with four wave frequencies corresponding to different $\frac{L_s}{\lambda}$ values ranging from 1 to 4. The $\frac{L_s}{\lambda}$ ratio, defined as R, is found to be one of the key factors that can be used to predict the motion shapes of a multibody system in waves.

From the time domain results shown in Figure 9(a), it can be seen that the array shapes exhibit periodic sinusoidal patterns, with the number of peaks or troughs equal to the R values. This implies that the system is excited by its (R+1)th eigen mode (except rigid body modes). To identify the significant frequency components of the time domain array shapes, a Fast Fourier Transform (FFT) is applied. Figure 9(b) shows the dominant frequencies, facilitating the examination of the array's performance under various wave frequencies. Resonance frequencies typically appear as higher amplitudes in the frequency spectrum, indicating the excitation at which the structure responds most vigorously.

It is observed that the excitation frequencies have an order that is proportional to its 2nd hinge-deflection mode (R=1), denoted as $0.077\times R$. The prominent peak in the frequency mode varies with the wave frequency: shorter waves stimulate higher mode frequencies, not necessarily confined to a single harmonic. In this study, where R is applied as 4.70, the exploration of mode frequencies extends up to the 6th order, with a notable emphasis on the 5th and 6th orders. This suggests that despite varying wave frequencies within the system, the continuous structure responds according to its inherent vibration behaviours.

It is worth noting that R is influenced by several factors such as the arrangement of the floating objects, their physical characteristics, and the stiffness of the connections. These factors need to be determined in advance before conducting evaluations.

As the R ratio increases, the structure is relatively longer to waves, it is seen that the modular solar system transits from multiple-rigid-body motions to a more flexible response, indicating that the modular system begins to experience greater internal stresses and deformations. This could result in larger cyclic loading on the connections between floaters. From an energy dissipation perspective, the rigid body responses indicate relative motions between floaters, which can dissipate more waves than a purely hydroelastic behaviour.

Mode	2	3	4	5	6
f(Hz)	0.077	0.154	0.231	0.307	0.384

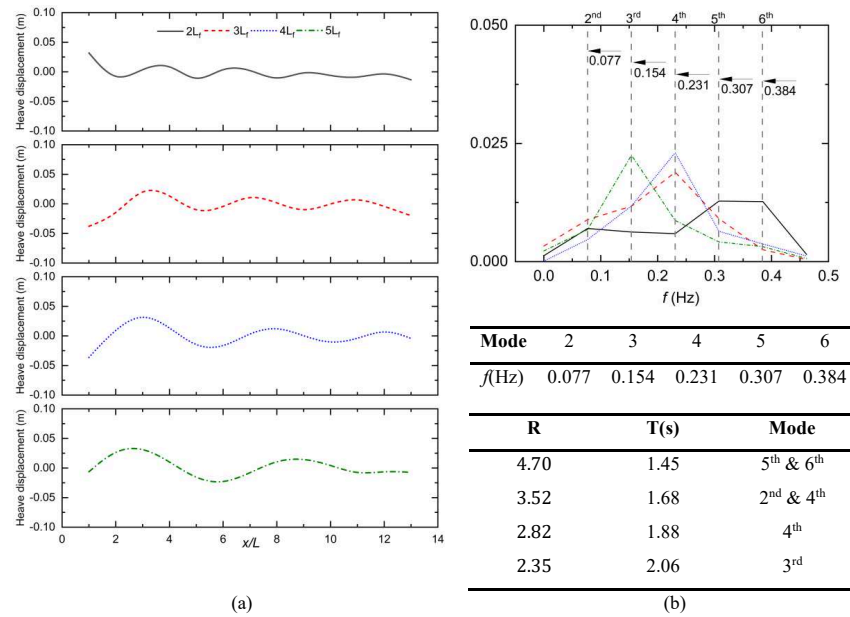| R	T(s)	Mode
4.70	1.45	5th & 6th
3.52	1.68	2nd & 4th
2.82	1.88	4th
2.35	2.06	3rd

(a) (b)

Figure 9: Vibration analysis and mode shapes on heave motion on frame column (C1) on various wave conditions, (a) Time domain results, (b) Vibration analysis.

To assess the vibration characteristics of the entire array, an advantage is taken of the symmetry at $y = 0$. Only one side of the array (C1 to C4) is taken into account. C1 represents the frame line, while C2-C4 represent the internal lines within the frame. The motion shapes and their vibration behaviours are examined in heading wave condition ($f = 0.714$Hz) with four even time frames within one wave cycle, as shown in Figure 10. Upon inspection from Figure 10(a), it becomes evident that the heave motion distributions do not coincide between frame and internal floaters, showcasing undulating shapes for each floater position occurring at the internal arrays.

The frequency modes of each column are shown in Figure 10(b). It is important to note that the resonance frequencies caused by the internal columns (C2-C4) may vary at specific time frame compared to those of the frame. The figure illustrates that the frame columns can induce a higher mode, reaching up to the 6th order in Figure 10(a), while the corresponding internal columns only reach the 5th order. The higher mode observed in the frame can be attributed to the mooring attachments. Further analysis is necessary and will be presented in future studies. Both the internal and frame columns consistently adhere to their eigenfrequencies regardless of wave conditions, with the magnitudes proportional to the R-th resonance mode and the system's 2nd eigenvalue (0.077). These findings emphasize the array motions in waves are mostly excited by their system eigenvalues, the motion pattern of the structure under changes in wave frequency may be roughly predicted by using the R value.
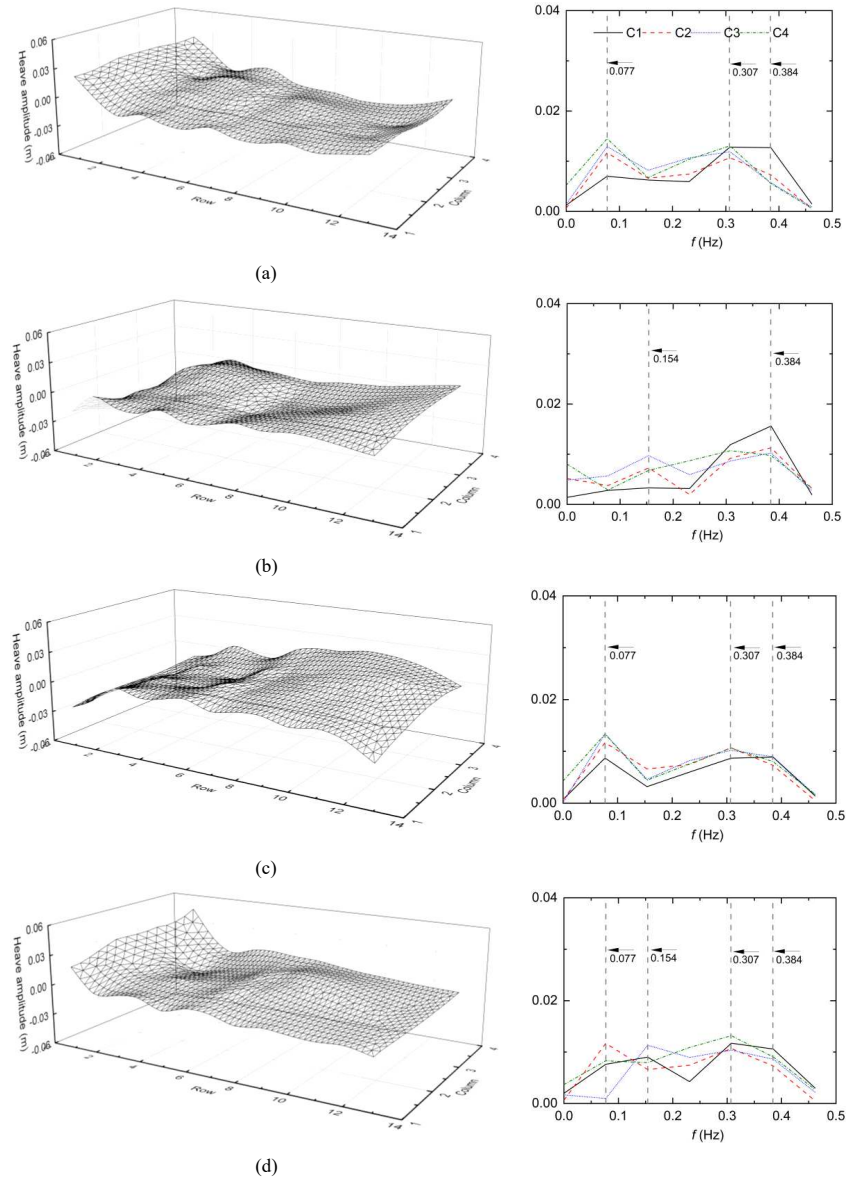
13

(a)

(b)

(c)

(d)

Figure 10: Vibration analysis of heave trajectory within array 13×7 at wave condition T=1.45s, time domain and vibration analysis at (a) t = nT + 0.25T, (b) t = nT + 0.5T, (c) t = nT + 0.75T, (d) t = $(n+1)T$.

14

5.3 Vibration analysis on pitch motions

Pitch motion is another important factor that greatly affects the efficiency of a MFS. This is mainly due to the potential deviation of the tilt angle, caused by sunlight absorption, from the optimal design alignment. Therefore, a similar approach is taken to assess different array deployments and expandability under various wave conditions. The time-average pitch RAOs of four array configurations (7×7, 9×7, 11×7, 13×7) are shown in Figure 11.

Similar trends are observed for pitch motion resulting from heave motions. Large rotations are associated with wave-ward and side-ward regions of the columns, and the magnitude decreases along with the wave propagation. However, rotational motions are greatly affected by the attaching hinge joints, with the largest magnitude being close to 0.5 at C1. In particular, the pitch motions of floaters located near fairlead positions are further controlled due to the restraining moments generated by the mooring lines. However, the present mooring cable assumes simple spring elements. It is recommended to apply more practical mooring codes for evaluations.
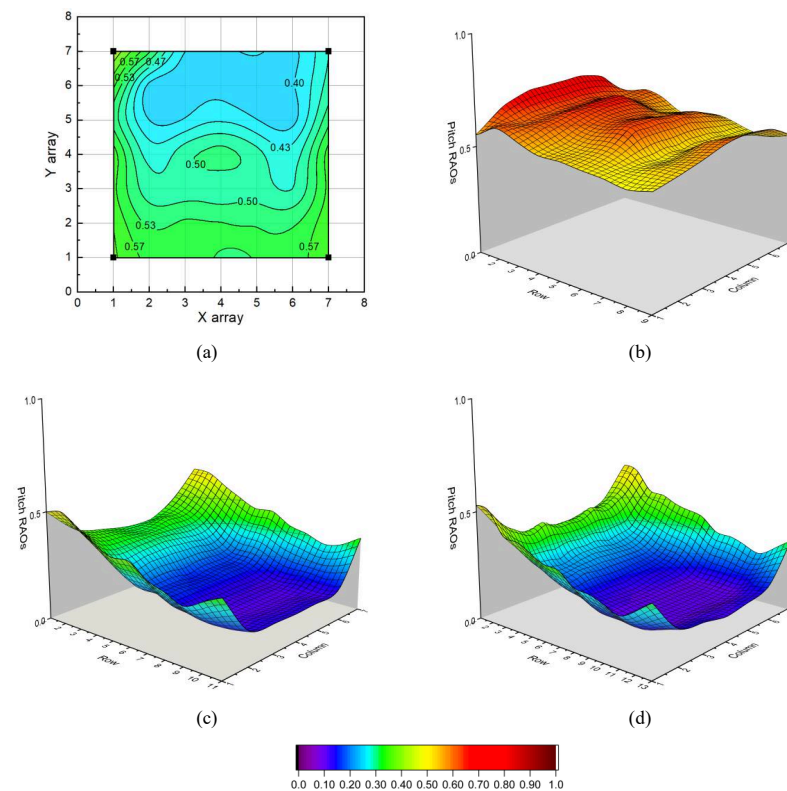

Figure 11: Pitch RAO distribution with various array distributions with waves, (a) Results of 7×7 array, (b) Results of 9×7 array, (c) Results of 11×7 array, (d) Results of 13×7 array.

Figure 12 illustrates the pitch distributions at the frame column (C=1) for varying column lengths (M=7, 9, 11, 13) across four time frames within one wave cycle under heading waves (T=1.453s). The longitudinal plots reveal periodic pitch motions influenced by the wavelength, akin to heave motions but with more pronounced effects. The sinusoidal curves align with the wave shapes and are accurately represented with the same phase shift as the waves. The sinusoidal curves align precisely with the wave shapes, exhibiting the same phase shift. This suggests

that the rotation of floating bodies in waves follows a sine wave pattern, closely mimicking the wave surface and causing the articulated multi-body structure to move in a flexible manner.

The pitch magnitude at the frame column is minimally affected by wave propagation, showing a slight decrease towards the middle point and emphasizing the two ends. This behaviour is attributed to the coupled effects of heave-pitch motions and the restraints imposed by the moorings. Notably, a hinge rotational stiffness of 0 is chosen to prevent inducing additional frequency within the system. It could result in the calculated pitch magnitude in this study being higher than what would be observed in practical scenarios.
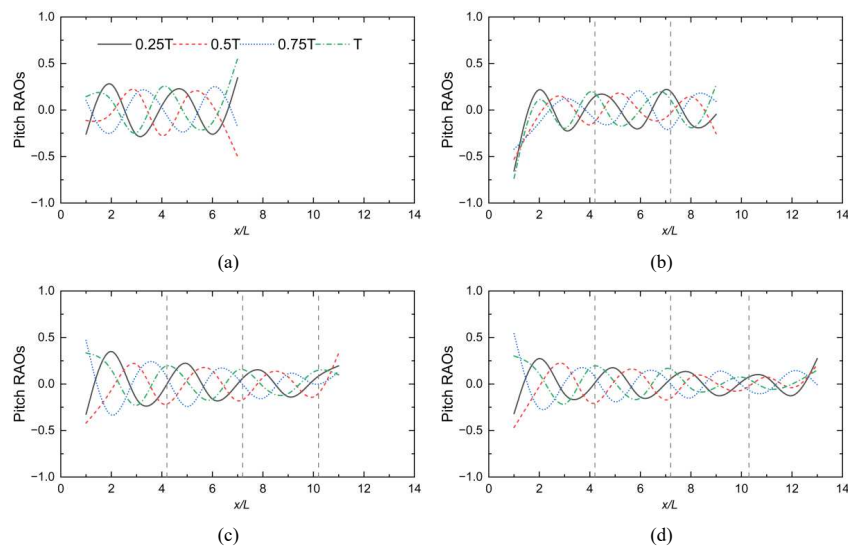

Figure 12: Pitch trajectory in longitudinal with four time frames at wave period $T = 1.45$s, (a) Results of 7×7 array, (b) Results of 9×7 array, (c) Results of 11×7 array, (d) Results of 13×7 array.

Figure 13 illustrates the pitch distribution of the first four columns (C=1-4) within four time frames in the wave cycle (T=1.45s), with the corresponding vibration analysis shown in Figure 13(b). The time domain results display steady and periodic patterns, and through FFT analysis, the high peak frequency components consistently appear at the 5th and 6th orders (0.307 and 0.384).

The peak vibration component signifies the incident wave causing system deformation; however, there is a distinction in how the modes are excited for the frame (C=1) and internal columns (C=2-4). Notably, the frame mode frequency consistently exhibits one order higher than the internal columns, mirroring a phenomenon observed in the heave shape vibration analysis. This suggests a consistent pattern of higher frequency excitation for the frame compared to the internal columns during pitch motion.
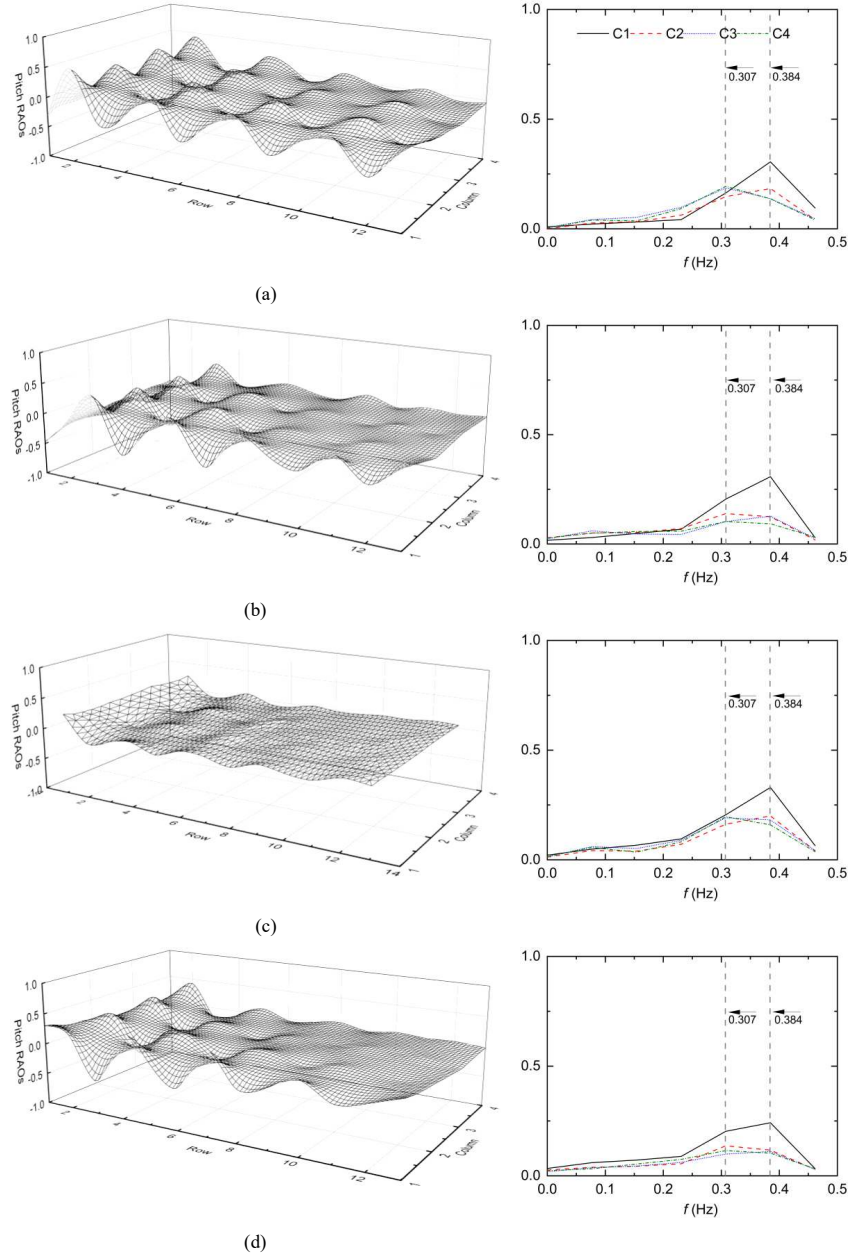
(a)

(b)

(c)

(d)

Figure 13: Vibration analysis of pitch trajectory within array 13×7 at wave condition T = 1.45s waves, time domain and vibration analysis at (a) t = nT + 0.25T, (b) t = nT + 0.5T, (c) t = nT + 0.75T, (d) t = $(n+1)T$.

Figure 14 presents the pitch distribution on a single array shape (13×7) at the frame column (C1) with four different R values ranging from 1 to 4, along with corresponding frequency results in Figure 14(b). The time domain results exhibit clear periods synchronized with incident waves, reminiscent of observations in heave motions.

In the prediction process, both heave and pitch can be anticipated similarly. The continuous array shapes are closely linked to the R value, where the deformation mode corresponds to R. Motion magnitudes can be roughly predicted based on the R value; for small R ($R=1$), the structure has a length similar to incident waves, and the entire structure moves in harmony with the wave shapes, behaving like a short and rigid body with seakeeping behaviour close to 1. Conversely, for large R, motion amplitudes are distinctly separated with an increase in modes. As a result, the overall array motion resembles the superposition of multiple frequencies. These findings support the reasonable prediction of array motions in monochromatic waves by defining R and natural frequencies initially. Such an approach can be beneficial during the initial design stage of the system, assisting in determining motion peaks using theoretical methods.

Increasing the mass and inertia of the modules would lower the global natural frequencies of the system, which could help avoid resonance. However, this would also induce increased loading as well as impact motion stability. Alternatively, optimising the buoyancy distribution and tuning the rod and hinge stiffnesses could be effective ways to mitigate resonance.

Mode	2	3	4	5	6
f(Hz)	0.077	0.154	0.231	0.307	0.384

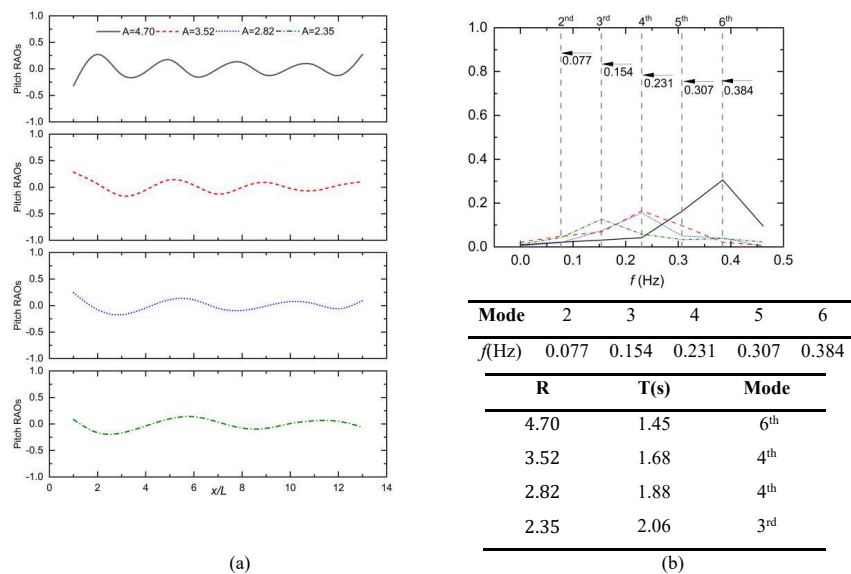| R	T(s)	Mode
4.70	1.45	6th
3.52	1.68	4th
2.82	1.88	4th
2.35	2.06	3rd

(a)　　　　　　　　　　　　　　(b)

Figure 14: Vibration analysis and mode shapes on pitch motion on frame column (C1) on various of wave conditions, (a) Time domain results, (b) Vibration analysis.

5.4 Potential of using a large hydroelastic body to represent multiple rigid bodies

The discretised articulated body approach exhibits continuum behaviours based on assumptions. To critically explore this, a comparative analysis is conducted involving three distinct concepts: an elastic beam solved using Finite Element Analysis (FEA), a discretised beam model solved through FVM, and a rigid-hinge body exhibiting stiffness characteristics. The tested cantilevered beam is fixed at two ends, with the primary focus on its resistance to self-deformation against gravitational forces.

The elastic beam in the FEA domain is characterized by its material properties (as shown in Table 4), with the discretized beam model in FVM adopting a methodical approach inspired by the differential equations governing beam deformations $K_{axial} = EA$ and $K_{bending} = EJ_y$, where J_y is the bending rigidity. A rigid-hinge-body, featuring an assumed axial stiffness of infinity ($K_{axial} = \infty$), provides a basis for restraining behaviours.

Figure 15 illustrates the deflection curves, serving as pivotal indicators for the structural response among the three conceptual frameworks. The exploration of static behaviour in local deformations incorporated considerations of shape variations. The progressive increase in the number of modules is observed to yield a smoothing effect on the beam deformation shapes. It is evident that the deflection closely converged to analytical solutions as the number of rigid modulus elements approaches infinite.

Table 4: Physical properties of the cantilever beam.

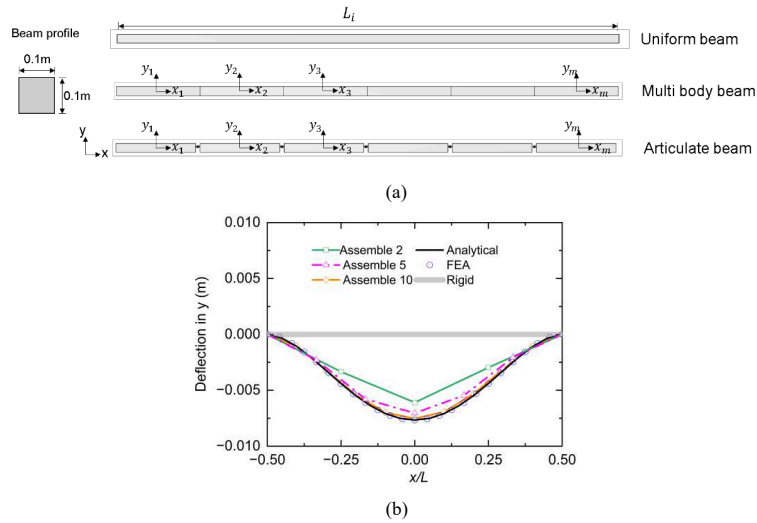| Properties	Unit	Value
Beam length L	m	1
Cross-section height	m	0.01
Cross-section thickness	m	0.01
Young's Modulus E	Gp_a	1.4
Poisson's Ratio	-	0.3

(a)

(b)

Figure 15: Comparison of three concepts of flexible beam modelling, (a) Various conceptual beams, (b) Deflection results.

6. Conclusions

Coastal and offshore developments of FPV systems can potentially benefit from modularised design to mitigate wave-induced structural issues. This study aimed to understand the motions of a modularised floating solar system under heading regular waves. A computational model based on the potential flow theory and multi-body dynamics was used. The effects of connection joints and mooring lines were also incorporated. The model revealed good accuracy by comparison with multibody dynamics in waves presented in (Chen et al., 2021; Chen et al., 2023). The hydrodynamic motions were examined for each floating solar unit at a series of wave conditions.

Based on a systematic analysis of simulation results, key findings include:

• The ratio of structure length to wavelength (R) is a crucial parameter governing the motions of the modular solar farm. Empirical relationships between R and the hydrodynamic response of each unit in an FPV array have been reported.

• The heave motion of an FPV array decreases from front units to rear units due to wave dissipation, whilst the pitch motion of marginal units is larger than internal units due to mooring effects.

• When R > 1, the motion characteristics of a large-scale modularised floating solar farm can be predicted by treating it as a continuous hydroelastic system. This allows approximating the complex multibody dynamics using a simplified approach.

The present potential flow method has limitations. It excludes nonlinear wave effects such as wave breaking, turbulence, and overwash. These limitations can be potentially remedied by developing Computational Fluid Dynamics and Multibody Dynamics approaches, e.g. (Li et al., 2022) and (Wei. et al., 2024b). The simplified linear spring mooring system could be unsuitable for a floating system in extreme conditions, such as rogue waves (Huang et al., 2022). Therefore, it is suggested to consider nonlinear mooring dynamics to overcome this limitation, e.g. (Wei et al., 2024a).

With advanced modelling methods developed to overcome present limitations, future research is recommended in the fields of structural resonance (Zhang. et al., 2023), extreme loading (McVicar et al., 2018), and wave energy dissipation (Huang et al., 2019). Wave energy dissipating when propagating through an array of structures is a highly interesting topic. In general, shorter waves will lose more energy in the array due to wave scattering, while this is complicated by the size of the gap between each unit. Further insights on this may be found in (Bennetts & Williams, 2015), (Porter, 2019), and (Montiel et al., 2024). In addition, regular wave conditions were used to enable physical analysis with straightforward parameterisation. However, it is important to note that sea states in reality are random and need to be considered in relevant engineering projects.

Acknowledgements:

Data availability:

All data underlying the results are available as part of the article and no additional source data are required.

References:

Anderlini, E., Husain, S., Parker, G. G., Abusara, M., & Thomas, G. (2020). Towards real-time reinforcement learning control of a wave energy converter. *Journal of Marine Science and Engineering*, *8*(11), 845.

Bennetts, L., & Williams, T. (2015). Water wave transmission by an array of floating discs. *Proceedings of the Royal Society A: Mathematical, Physical and Engineering Sciences*, *471*(2173), 20140698.

Bi, C., & Law, A. W.-K. (2023). Co-locating offshore wind and floating solar farms–Effect of high wind and wave conditions on solar power performance. *Energy*, *266*, 126437.

Cao, Y., Cao, D., He, G., Ge, X., & Hao, Y. (2021). Modelling and vibration analysis for the multi-plate structure connected by nonlinear hinges. *Journal of Sound and Vibration*, *492*. https://doi.org/10.1016/j.jsv.2020.115809

Cazzaniga, R., Cicu, M., Rosa-Clot, M., Rosa-Clot, P., Tina, G., & Ventura, C. (2018). Floating photovoltaic plants: Performance analysis and design solutions. *Renewable and Sustainable Energy Reviews*, *81*, 1730-1741.

Cazzaniga, R., & Rosa-Clot, M. (2021). The booming of floating PV. *Solar Energy*, *219*, 3-10. https://doi.org/10.1016/j.solener.2020.09.057

Chen, M., Guo, H., Wang, R., Tao, R., & Cheng, N. (2021). Effects of Gap Resonance on the Hydrodynamics and Dynamics of a Multi-Module Floating System with Narrow Gaps. *Journal of Marine Science and Engineering*, *9*(11). https://doi.org/10.3390/jmse9111256

Chen, M., Ouyang, M., Guo, H., Zou, M., & Zhang, C. (2023). A Coupled Hydrodynamic–Structural Model for Flexible Interconnected Multiple Floating Bodies. *Journal of Marine Science and Engineering*, *11*(4). https://doi.org/10.3390/jmse11040813

Choi, Y. K., & Lee, J. H. (2015). Structural Safety Assessment of Ocean-Floating Photovoltaic Structure Model. *Israel Journal of Chemistry*, *55*(10), 1081-1090. https://doi.org/10.1002/ijch.201400197

Claus, R., & López, M. (2022). Key issues in the design of floating photovoltaic structures for the marine environment. *Renewable and Sustainable Energy Reviews*, *164*. https://doi.org/10.1016/j.rser.2022.112502

Cummins, W. (1962). The impulse response function and ship motions.

Dafnakis, P., Bhalla, A. P. S., Sirigu, S. A., Bonfanti, M., Bracco, G., & Mattiazzo, G. (2020). Comparison of wave–structure interaction dynamics of a submerged cylindrical point absorber with three degrees of freedom using potential flow and computational fluid dynamics models. *Physics of Fluids*, *32*(9).

Dai, J., Zhang, C., Lim, H. V., Ang, K. K., Qian, X., Wong, J. L. H., Tan, S. T., & Wang, C. L. (2020). Design and construction of floating modular photovoltaic system for water reservoirs. *Energy*, *191*. https://doi.org/10.1016/j.energy.2019.116549

Delacroix, S., Bourdier, S., Soulard, T., Elzaabalawy, H., & Vasilenko, P. (2023). Experimental Modelling of a Floating Solar Power Plant Array under Wave Forcing. *Energies*, *16*(13). https://doi.org/10.3390/en16135198

Esparza, I., Olábarri Candela, Á., Huang, L., Yang, Y., Budiono, C., Riyadi, S., Hetharia, W., Hantoro, R., Setyawan, D., & Utama, I. (2024). Floating PV Systems as an Alternative Power Source: Case Study on Three Representative Islands of Indonesia. *Sustainability*, *16*(3), 1345.

Essak, L., & Ghosh, A. (2022). Floating Photovoltaics: A Review. *Clean Technologies*, *4*(3), 752-769. https://doi.org/10.3390/cleantechnol4030046

Fang, M., & Kim, C. (1986). Hydrodynamically coupled motions of two ships advancing in oblique waves. *Journal of ship research*, *30*(03), 159-171.

Feng, X., Bai, W., Chen, X., Qian, L., & Ma, Z. (2017). Numerical investigation of viscous effects on the gap resonance between side-by-side barges. *Ocean Engineering*, *145*, 44-58.

Hong, S., Kim, J., Cho, S., Choi, Y., & Kim, Y. (2005). Numerical and experimental study on hydrodynamic interaction of side-by-side moored multiple vessels. *Ocean Engineering*, *32*(7), 783-801.

Huang, L., Li, Y., Benites-Munoz, D., Windt, C. W., Feichtner, A., Tavakoli, S., Davidson, J., Paredes, R., Quintuna, T., & Ransley, E. (2022). A review on the modelling of wave-structure interactions based on OpenFOAM. *OpenFOAM® Journal*, *2*, 116-142.

Huang, L., Ren, K., Li, M., Tuković, Ž., Cardiff, P., & Thomas, G. (2019). Fluid-structure interaction of a large ice sheet in waves. *Ocean Engineering*, *182*, 102-111.

Ikhennicheu, M., Blanc, A., Danglade, B., & Jean-Christophe, G. (2022). OrcaFlex Modelling of a Multi-Body Floating Solar Island Subjected to Waves. *Energies*, *15*(23), Article 9260. https://doi.org/10.3390/en15239260

Jiang, Z., Dai, J., Saettone, S., Tørå, G., He, Z., Bashir, M., & Souto-Iglesias, A. (2023). Design and model test of a soft-connected lattice-structured floating solar photovoltaic concept for harsh offshore conditions. *Marine Structures*, *90*, 103426.

Kjeldstad, T., Lindholm, D., Marstein, E., & Selj, J. (2021). Cooling of floating photovoltaics and the importance of water temperature. *Solar Energy*, *218*, 544-551.

Kjeldstad, T., Nysted, V. S., Kumar, M., Oliveira-Pinto, S., Otnes, G., Lindholm, D., & Selj, J. (2022). The performance and amphibious operation potential of a new floating photovoltaic technology. *Solar Energy*, *239*, 242-251. https://doi.org/10.1016/j.solener.2022.04.065

Li, A.-j., & Liu, Y. (2022). Hydrodynamic performance and energy absorption of multiple spherical absorbers along a straight coast. *Physics of Fluids*, *34*(11).

Li, X., Xiao, Q., Zhou, Y., Ning, D., Incecik, A., Nicoll, R., ... & Campbell, D. (2022). Coupled CFD-MBD numerical modeling of a mechanically coupled WEC array. *Ocean Engineering*, *256*. https://doi.org/10.1016/j.oceaneng.2022.111541

Li, Z., Chen, D., & Feng, X. (2023). Hydroelastic and expansibility analysis of a modular floating photovoltaic system with multi-directional hinge connections. *Ocean Engineering*, *289*, 116218.

Liu, Y., Ren, N., & Ou, J. (2022). Hydrodynamic analysis of a hybrid modular floating structure system under different wave directions. *Applied Ocean Research*, *126*. https://doi.org/10.1016/j.apor.2022.103264

McVicar, J., Lavroff, J., Davis, M. R., & Thomas, G. (2018). Fluid–structure interaction simulation of slam-induced bending in large high-speed wave-piercing catamarans. *Journal of Fluids and Structures*, *82*, 35-58.

Michailides, C., Loukogeorgaki, E., & Angelides, D. C. (2013). Response analysis and optimum configuration of a modular floating structure with flexible connectors. *Applied Ocean Research*, *43*, 112-130. https://doi.org/10.1016/j.apor.2013.07.007

Montiel, F., Meylan, M., & Hawkins, S. (2024). Scattering kernel of an array of floating ice floes: application to water wave transport in the marginal ice zone. *Proceedings of the Royal Society A*, *480*(2282), 20230633.

Newman, J. (1997). Wave effects on hinged bodies. Part I—body motions. In: technical report (www. wamit. com).

Newman, J. N. (1994). Wave effects on deformable bodies. *Applied Ocean Research*, *16*(1), 47-59.

Newman, J. N. (2005). Efficient hydrodynamic analysis of very large floating structures. *Marine Structures*, *18*(2), 169-180. https://doi.org/10.1016/j.marstruc.2005.07.003

Ohkusu, M. (1976). The analysis of wave forces acting upon multifloat-supported platforms. *Trans West Japan Soc Naval Arch*, *51*, 153-170.

Porter, R. (2019). The coupling between ocean waves and rectangular ice sheets. *Journal of Fluids and Structures*, *84*, 171-181.

Ren, N., Zhang, C., Magee, A. R., Hellan, Ø., Dai, J., & Ang, K. K. (2019). Hydrodynamic analysis of a modular multi-purpose floating structure system with different outermost connector types. *Ocean Engineering*, *176*, 158-168. https://doi.org/10.1016/j.oceaneng.2019.02.052

Sahu, A., Yadav, N., & Sudhakar, K. (2016). Floating photovoltaic power plant: A review. *Renewable and Sustainable Energy Reviews*, *66*, 815-824. https://doi.org/10.1016/j.rser.2016.08.051

Shi, W., Yan, C., Ren, Z., Yuan, Z., Liu, Y., Zheng, S., Li, X., & Han, X. (2023). Review on the development of marine floating photovoltaic systems. *Ocean Engineering*, *286*, 115560.

Sree, D. K., Law, A. W.-K., Pang, D. S. C., Tan, S. T., Wang, C. L., Kew, J. H., Seow, W. K., & Lim, V. H. (2022). Fluid-structural analysis of modular floating solar farms under wave motion. *Solar Energy*, *233*, 161-181.

Wang, C., Xu, H., Zhang, Y., & Chen, W. (2023). Hydrodynamic investigation on a three-unit oscillating water column array system deployed under different coastal scenarios. *Coastal Engineering*, 104345.

Wang, C., Zheng, S., & Zhang, Y. (2022). A heaving system with two separated oscillating water column units for wave energy conversion. *Physics of Fluids*, *34*(4).

Wang, J., & Lund, P. D. (2022). Review of Recent Offshore Photovoltaics Development. *Energies*, *15*(20). https://doi.org/10.3390/en15207462

Wei, Y., Yu, S., Jin, P., Huang, L., Elsherbiny, K., & Tezdogan, T. (2024a). Coupled analysis between catenary mooring and VLFS with structural hydroelasticity in waves. *Marine Structures*, *93*, 103516.

Wei., Y., Yu, S., Li, X., Zhang, C., Ning, D., & & Huang, L. (2024b). Hydrodynamic analysis of a heave-hinge wave energy converter combined with a floating breakwater. *Ocean Engineering*, *293*, 116618.

Zhang, D., Du, J., Yuan, Z., Yu, S., & Li, H. (2023). Motion characteristics of large arrays of modularized floating bodies with hinge connections. *Physics of Fluids*, *35*(7).

Zhang, D., Yuan, Z.-M., Du, J., & Li, H. (2022). Hydrodynamic modelling of large arrays of modularized floating structures with independent oscillations. *Applied Ocean Research*, *129*. https://doi.org/10.1016/j.apor.2022.103371

Zhang., Wang, P., Huang, L., Zhang, M., Wu, H., & & Ning, D. (2023). Resonance mechanism of hydroelastic response of multi-patch floating photovoltaic structure in water waves over stepped seabed. *Physics of Fluids*, *35*(10).

Zhu, H.-r., Zhu, R.-c., & Miao, G.-p. (2008). A time domain investigation on the hydrodynamic resonance phenomena of 3-D multiple floating structures. *Journal of Hydrodynamics*, *20*(5), 611-616.